Biomechanics of the acetabular cup implant Influence of anisotropic bone properties on the biomechanical behavior of the acetabular cup implant: a multiscale finite element study

Vu-Hieu Nguyen, Giuseppe Rosi, Salah Naili, Adrien Michel, Maria-Letizia Raffa, Romain Bosc, Jean-Paul Meningaud, Christine Chappard, Naoki Takano, Guillaume Haiat

Influence of anisotropic bone properties on the biomechanical behavior of the acetabular cup implant: a multiscale finite element study

Vu-Hieu Nguyen,
Giuseppe Rosi,
Salah Naili
Adrien Michel
Maria-Letizia Raffa
Université Paris-Est, Laboratoire de Modélisation et de Simulation MultiEchelle,
UMR CNRS 8208, 61 avenue du général de Gaulle, Créteil 94010 cedex, France
Romain Bosc, Jean-Paul Meningaud,
Université Paris-Est, INSERM U955, Equipe 10, 8 rue du Général Sarrail,
94010 Créteil Cedex, France
Christine Chappard
CNRS, Université Paris Diderot, Laboratoire Bioingénierie Biomécanique Ostéo-Articulaires,
UMR CNRS 7052, Paris, France
Naoki Takano,
Keio University, Faculty of Science and Engineering, Department of Mechanical Engineering
3-14-1 Hiyoshi, Kohoku-ku, Yokohama, Kanagawa, Japan
Guillaume Haiat,
CNRS, Laboratoire de Modélisation et de Simulation Multi-Echelle,
UMR CNRS 8208, 61 avenue du général de Gaulle, Créteil 94010, France
École de technologie supérieure, 1100 Notre-Dame Street West, Montreal, QC H3C 1K3,
Canada; Research Center, Hôpital du Sacré-Cœur de Montréal, 5400, Gouin Boul. West,
Montreal, QC H4J 1C5, Canada
Corresponding author:
Guillaume HAÏAT
Laboratoire de Modélisation et de Simulation Multi Echelle, UMR CNRS 8208,
61 avenue du Général de Gaulle, 94010 Créteil cedex, France
tel : (33) 1 45 17 14 41 fax : (33) 1 45 17 14 33
e-mail : guillaume.haiat@univ-paris-est.fr
Submitted to CMBBE

Abstract

Although the biomechanical behavior of the acetabular cup (AC) implant is determinant for the surgical success, it remains difficult to be assessed due to the multiscale and anisotropic nature of bone tissue. The aim of the present study was to investigate the influence of the anisotropic properties of peri-implant trabecular bone tissue on the biomechanical behavior of the AC implant at the macroscopic scale.

Thirteen bovine trabecular bone samples were imaged using micro-computed tomography (μCT) with a resolution of 18 μm. The anisotropic biomechanical properties of each sample were determined at the scale of the centimeter based on a dedicated method using asymptotic homogenization. The material properties obtained with this multiscale approach were used as input data in a 3D finite element model to simulate the macroscopic mechanical behavior of the AC implant under different loading conditions.

The largest stress and strain magnitudes were found around the equatorial rim and in the polar area of the AC implant. All macroscopic stiffness quantities were significantly correlated (R^2>0.85, p<6.5 e-6) with BV/TV (bone volume/total volume). Moreover, the maximum value of the von Mises stress field was significantly correlated with BV/TV (R^2>0.61, p<1.6 e-3) and was always found at the bone-implant interface. However, the mean value of the microscopic stress (at the scale of the trabeculae) decrease as a function of BV/TV for vertical and torsional loading and do not depend on BV/TV for horizontal loading. These results highlight the importance of the anisotropic properties of bone tissue.

Keywords: Acetabular cup; total hip replacement; finite element analysis; bone; Homogenization

1. Introduction

While hip arthroplasty has become a common surgical intervention with more than 450,000 interventions each year in the USA [1], failures still occur, leading to dramatic consequences. Aseptic loosening is one of the most common causes of failure [2, 3] and is related to the implant biomechanical behavior. The long-term fixation of the acetabular cup (AC) implant is obtained through osseointegration phenomena [4, 5], which leads to a bonded bone-implant interface after the bone healing process. Load transfers at the bone-implant interface are complex due to i) their multiaxial nature (caused by body weight bearing), ii) the complex multiscale properties of bone tissue (in particular, bone is an anisotropic material) and iii) the evolving properties of bone tissue due to remodeling phenomena. The determination of the biomechanical behavior of the AC implant is important to assess its stability and to understand osseointegration phenomena [6, 7] around the implant [8]. Nowadays, the surgeons rely on their proprioception to assess empirically the AC implant stability by applying manually forces and/or torques to the ancillary.

Coupling three-dimensional images obtained with micro-computed tomography (µCT) and numerical simulation has allowed the development of biomechanical analyses taking into account the influence of the bone microstructure on implants behavior [9, 10]. Peri-implant bone microarchitecture has been shown to play an important role in the distribution of stresses by forming load transfer paths [11, 12]. Bone properties also determine the dynamic implant pull-out force [13]. To analyze the properties of peri-implant bone tissue, biomechanical investigations based on the trabecular bone structure are necessary. However, none of the aforementioned studies have investigated so far the AC implant behavior. The difficulty lies in the size of the AC implant, that requires to take into account a large volume of trabecular bone in the computation, which explain why, to the best of our knowledge, classical micro-finite element analyses taking into account bone microstructure around the implant have not been applied to study the mechanical behavior of the AC implant.

Numerous studies focused on the effect of the AC implant shape [14-17], material [18] and surface treatment [2] on its biomechanical properties. However, the relation between trabecular bone properties and the AC implant macroscopic mechanical behavior remains poorly established [19]. Moreover, the effect of the anisotropic nature of bone tissue as well as the distribution of the stress and strain fields around an AC implant remains unknown. Several models have been developed to assess the deformation of the AC implant and the stability obtained after the press-fit insertion [20, 21]. Other numerical studies have computed the stress field in peri-implant bone tissue while the AC implant was progressively implanted and identified the AC periphery as the zone with the highest stresses due to the press-fit configuration [16, 20]. Our group has developed a method that can provide information on the implant insertion conditions based on the variation of the force applied between the hammer and the ancillary as a function of time [22-25]. However, trabecular

bone was modeled as an isotropic medium in all the aforementioned studies and the effect of the peri-implant bone properties on the implant mechanical behavior at the macroscopic level has not yet been studied. Investigating the AC implant mechanical behavior is an important problem because it may help to better understand implant failures as well as osseointegration phenomena.

The aim of this work is to study the influence of the peri-implant anisotropic bone mechanical properties on the mechanical behavior of the AC implant. In particular, we aim at studying the distribution of the strain and stress fields around an AC implant when anisotropic material properties are considered and at investigating the relation between bone properties and the AC implant macroscopic behavior. The proposed approach consists in coupling numerical simulation tools with high resolution imaging techniques and multiscale analyses in order to understand the determinants of the biomechanical behavior of the AC implant under physiological conditions. Stress and strain distributions in the homogenized peri-implant bone are computed for different loading conditions of the AC implant.

2. Material and methods

The general strategy employed herein is summarized in Fig. 1 and is described in more details below. The first step consists in the measurement of the microarchitecture of thirteen bone samples, which was used as input data in a homogenization procedure, leading to the determination of homogenized properties at the scale of the centimeter. These anisotropic material properties were then used in a finite element model to determine the macroscopic stiffness of the bone-implant system. All loads were applied through a bar protruding from the implant, which models the ancillary, because it corresponds to a simple situation of clinical interest (in particular when surgeons assess manually the AC implant stability). From the viewpoint of the computational cost and memory requirements, it remains difficult to consider the bone microstructure directly in the finite element computations due to the size of the AC implant, which justifies the use of homogenized bone properties. Such approach is therefore useful to consider the effect of the microstructure of trabecular bone in the numerical analyses.

2.1. Determination of the homogenized bone properties

Bone samples imaging

Thirteen trabecular bone samples were obtained from bovine femurs similarly as what was done in [26]. The samples were then cut in the proximal region in order to obtain cubic specimens (with a size of approximately 10*10*10 mm) using an electric saw. A X-ray µCT device (Skyscan1176® scanner,

Skyscan, Kontich, Belgium) was used to obtain the 3-D image of each bone sample with a resolution of 18 µm. The CT images were then binarized to separate the image into bone tissue and bone marrow. The value of BV/TV (bone volume fraction) was then determined for each sample.

Homogenization method

The binarized 3D images were used as input data in the homogenization procedure described in more details in [27] and in the appendix. Numerical models were automatically generated using 18 µm sized voxel elements to determine the homogenized stiffness coefficients at the scale of the sample. For the mesh generation and analysis, the Voxelcon software (Quint Corp., Fuchu, Tokyo, Japan) was used, in which a two-scale homogenization method based on the asymptotic expansion theory was implemented [28, 29]. The interest of this homogenization method lies in that it can take into account the influence of any complex micro-architecture on the macroscopic properties of the bone-implant system. Using this approach, trabecular bone regions can be replaced by regions with homogenized material properties, which can in turn be discretized by coarse finite elements. The size of each microstructure model (or representative volume element; RVE) ranged from approximately 5.5 mm to 9.8 mm, which was large enough to represent the complex and random heterogeneity. The number of voxel finite elements of each RVE ranged from approximately 9 to 23 millions. 3-D periodic boundary conditions were applied to the numerical model to obtain the homogenized properties by solving a self-equilibrium problem based on the two-scale homogenization method. Theoretically, a scale ratio between macro- and micro-scales is assumed first and assigned to the principal of virtual work. Next, the averaging principle is used by taking the limit of zero ratio in order to split the problem into macro- and microscopic equations and to define the homogenized (averaged) properties [28,29]. Table 1 shows the material properties used for bone tissue in each RVE.

The output of the homogenization procedure provides a stiffness tensor $\boldsymbol{C^o}$, which was defined according to the local axes of the original sample. However, since the axes of the samples did not necessarily coincide to the principal directions of anisotropy, a rotation procedure was applied to the stiffness tensor in order to determine its principal directions. The required rotation was defined by maximizing the coefficient $C^0{}_{3333}$ and minimizing the coefficient $C^0{}_{1111}$. The aim of this rotation procedure was to obtain the stiffness tensor for which the principal direction associated with $C^0{}_{3333}$ is aligned with the *z*-axis, similarly as in physiological conditions. Here, the z-axis of the model is aligned with the stiffest principal direction of the homogenized elasticity tensor because the main trabecular orientation, which corresponds to the stiffest principal direction of the homogenized elasticity tensor, follows the main direction of the stresses applied *in vivo*, due to remodeling phenomena [30]. The main orientation of the mechanical stresses can be assumed to be oriented along the axis of the AC implant, which can be explained by simple gait analyses. The rotated homogenized stiffness tensor was computed as described in details in [31], leading to the determination of

the stiffness tensor $\boldsymbol{C^H}$, which is used as input data in the macroscopic finite element model (FEM) described below. This rotation procedure results in a main trabecular orientation parallel to the z axis, which corresponds to a situation of interest due to load bearing constraints.

2.2 Geometry and material properties

A 3D FEM was employed to simulate the mechanical behavior of an AC implant inserted in trabecular bone tissue similarly as what was done in [32], which corresponds to a validation of the computational method. Figure 2 shows the geometrical configuration which consists of three subdomains: trabecular bone Ω_t, the AC implant (merged with a bar representing the ancillary) Ω_{ac} and cortical bone Ω_c. The origin of the z-axis is taken in the top region of the system.

The implant and bone sizes were chosen similarly as in previous studies [25, 33, 34]. Based on typical AC implants used in the clinic, the cup was designed as a cobalt-chromium alloy with an inside diameter of 50 mm and a wall thickness of 4 mm (see Fig. 2). Trabecular (Ω_t, 21 mm thickness) and cortical (Ω_c, 2 mm thickness) bone regions were defined as hemispheric cups around the AC implant. All subdomains are assumed to be homogeneous and to have a linear elastic behavior. While cortical bone and the cobalt chromium cup were assumed to be isotropic (see Table 1), trabecular bone was assumed to be anisotropic. For each sample, the mechanical properties obtained after the application of the homogenization procedure described in subsection 2.1 were used for trabecular bone.

2.3. Numerical simulation method

The macroscopic problem was solved using the Ansys software (ANSYS Inc., Canonsburg, PA, USA). Twenty-noded elements were used to mesh the simulation domain, resulting in around 130,000 elements. A 20 nodes element with quadratic approximation was employed because it is suitable to represent the curved boundaries by a piecewise-quadratic approximation. A mesh sensitivity study to determine the mesh size which provide converged finite element solutions (data not shown). Small displacement assumptions were used in order to simulate the mechanical behavior of the system. The problem is solved following the classical equation of elasticity at equilibrium considered for each subdomain and by neglecting body forces, which correspond to $\nabla . \boldsymbol{\sigma} = \mathbf{0}$ in Ωt, Ωac and Ωc, where $\nabla .$ is the divergence operator and $\boldsymbol{\sigma}$ is the stress tensor.

The boundary of each sub-domain is divided into different parts corresponding to the nature of the boundary condition: with imposed traction on Γ_α^σ, imposed displacement on Γ_α^u or with interface conditions on Γ_α^i ($\Gamma_\alpha = \Gamma_\alpha^\sigma \cup \Gamma_\alpha^u \cup \Gamma_\alpha^i$) as shown in Fig. 2.

Bone tissue is fixed on the outer circle located at the top surface of cortical bone (see Fig. 2). Therefore the boundary condition imposed on this line Γ_c^u is given by:

$$\boldsymbol{u} = \mathbf{0} \qquad \text{on } \Gamma_c^u. \tag{1}$$

where $\boldsymbol{u}$ is the displacement field vector.

Continuity conditions of traction and of displacement were assumed on Γ_α^i, which corresponds to the interfaces between Ω_{ac} and Ω_t, and between Ω_t and Ω_c. These conditions represent fully bonded interfaces, which will be discussed in Section 4.

All boundary conditions in Γ_α^σ except in Γ_{ac}^σ (see Fig. 2) were considered as free boundary conditions given by:

$$\boldsymbol{\sigma n} = \mathbf{0} \tag{2}$$

where $\boldsymbol{n}$ is the normal unit vector of the three subdomains Ω_t, Ω_{ac} and Ω_c.

The movement of the system is governed by the stresses applied to Γ_{ac}^σ, which corresponds to the circular part of upper part of Ω_{ac}. Four different loading conditions were successively considered based on physiological conditions described in [16, 35]. First, an axial loading in the *z*-direction consisted in applying a load of F_z =1000 N to the top of the bar. Then, a torsional loading (T_z) of 20 N.m was applied to the top of the bar. Eventually, two horizontal loadings consisted in applying horizontal forces (F_x and F_y) of 1000 N to the top of the bar along the *x*- and *y*-directions. The forces F_x and F_y were homogeneously applied to the top of the bar.

2.4. Data analysis

The mechanical behavior of the AC implant was described by macroscopic stiffness quantities, which are defined according to the type of loading conditions. Moreover, the effect of the anisotropic properties was assessed qualitatively by plotting the von Mises stresses and the strain field for the various loading conditions described below. The stress field was determined at Gauss points.

When considering the vertical loading condition (application of F_z), the implant stiffness S_z was defined based on the vertical displacement d_z of the point located on the axis of symmetry of the AC implant and at the interface between bone tissue and the implant by:

$$S_Z = \frac{F_z}{d_z}. \tag{3}$$

For the torsional loading (application of T_z), the implant stiffness S_θ was defined based on the rotation angle θ_z of the AC implant by:

$$S_\theta = \frac{T_z}{\theta_z}. \quad (4)$$

For the horizontal loading along the *x*-axis (respectively *y*-axis), the implant stiffness S_x (respectively S_y) was defined based on the displacement d_x in the *x*-direction (respectively d_y in the *y*-direction) of the points located on the axis of symmetry of the AC implant and at the interface between bone tissue and the implant by:

$$S_x = \frac{F_x}{d_x} \text{ (respectively } S_y = \frac{F_y}{d_y}\text{).} \quad (5)$$

The relationship between each quantity defined above (corresponding to the macroscopic stiffness of the AC implant) and BV/TV was studied using a linear regression analysis.

Moreover, for each sample and each loading condition, all components of the stress and strain tensors were determined and the von Mises stress field was then determined. The maximum value of the von Mises stress was then determined for each sample and each loading condition.

3. Results

Figure 3 shows the relationship between the different macroscopic stiffness properties (S_z, S_θ, S_x and S_y, obtained for the four loading conditions) and BV/TV. All macroscopic stiffness properties are shown to increase significantly as a function of BV/TV (R^2 >0.85, p<6.5 e-6), because the rigidity of trabecular bone tissue increases as a function of BV/TV (see section 4 for further details).

Figure 4 shows the relationship between the maximum value of the von Mises stress (noted $<\sigma_{Macro}>$) obtained in the entire trabecular region (Ω_t) for the four loading conditions and BV/TV. Again, for all loading scenarios, the maximum value of the von Mises stress is shown to increase significantly as a function of BV/TV (R^2 >0.61, p<1.6 e-3),which will be explained in section 4.

Figure 5 shows the cartography of the von Mises stresses for a sample with a BV/TV value equal to 18% (which was chosen because it corresponds to typical values found in the acetabulum) in the plane Π_{yz}

in the AC implant and in the peri-implant bone tissue under vertical, torsional and horizontal loading along the *x*-axis. Figure 5 shows that all stress fields are not symmetric compared to the *z*-axis, which can be explained by the anisotropic properties of bone tissue.

Figure 6 shows the cartography of the von Mises stresses for the same sample obtained by cutting the sample in the plane Π_{xy} corresponding *z*= -26.5 mm (the origin *z*=0 corresponding to Γ_u^c, *i.e.* the upper end of cortical bone where the boundary conditions correspond to fixed displacements). For each image, two regions of interest (ROI) can be distinguished. The first ROI corresponds to the outer part of the image and shows the cartography of the von Mises stresses in bone tissue located in the plane Π_{xy}. The second ROI corresponds to the inner part of the image and shows the projection of the von Mises stresses obtained in the bone-implant interface located under Π_{xy} (*i.e.* for $z < -26.5$mm) on Π_{xy}. The results are shown under vertical loading (a), torsional loading (b) and horizontal loading along the *x*-axis (c). Figures 6 a) and 6 b) show that even if the applied loading and geometry of the structure are symmetric with respect to the z-axis, the resulting stress fields are not symmetric due to the anisotropy of trabecular bone tissue. Similarly, Fig. 6 c) shows that the stress field is not symmetric compared to the *x*-axis, which can also be explained by the anisotropic properties of bone tissue.

Figure 7 shows the cartography of different components of the strain tensor $\boldsymbol{\varepsilon}$ in the vertical loading configuration. Figure 7a) (respectively 7b) and 7c)) shows the results corresponding to ε_{zz} (respectively ε_{yz} and ε_{xz}) obtained in the plane Π_{yz}. Figure 7d) shows the results corresponding to ε_{xz} obtained in the plane Π_{xz}. Again, Fig. 7 a) shows that the strain field is not symmetric compared to the *z*-axis, which can also be explained by the anisotropic properties of bone tissue.

Figure 8 shows the cartography of different components of the strain sensor in the torsional loading configuration. Figure 8a) (respectively 8b)) shows the results corresponding to ε_{zz} (respectively ε_{xz}) obtained in the plane Π_{yz}. Moreover, Figure 8c) (respectively 8d)) shows the results corresponding to ε_{zz} (respectively ε_{yz}) obtained in the plane Π_{xz}.

Figure 9 shows the cartography of different components of the strain sensor in the horizontal loading configuration along the x-axis. Figure 9a) (respectively 9b), 9c) and 9d)) shows the results corresponding to ε_{xx} (respectively ε_{xz}, ε_{yz}, and $|\varepsilon_{xy}|$) obtained in the plane Π_{yz}. Figure 9 b) shows that the strain field is not symmetric compared to the *z*-axis, which can be explained by the anisotropic properties of bone tissue.

4. Discussion

The approach carried out in the present study may be compared with other works published in the literature. Micro-finite element analyses (see for example [36]), which consist in converting trabecular bone µCT images into finite element models has now become a routine procedure in bone biomechanics. However, such approaches are difficult to be carried out at the scale of the AC implant due to the huge computational power required to account for the trabecular bone microstructure in the entire volume of interest. Approaches based on micromechanics constitute alternative methods to model the multiscale properties of bone tissues [37, 38]. For example, methods involving micromechanics-based conversion of µCT data into anisotropic elasticity tensors were applied to the mandible [39] and to human femoral bone [40]. However, the microstructure of trabecular bone was taken into account through an average rule of the X-ray attenuation coefficients. A similar approach has been carried out in [41, 42] but bone tissue was modeled as an isotropic material.

While studying the effect of impingement on stresses at the bone-implant interface, Voigt et al. [42] found similar level of stresses in bone tissue. Differences between the various models in terms of geometrical configurations and bone mechanical properties may explain the slight variations in stress fields and magnitude [42], which remain however difficult to quantify due to the difference in terms of geometrical configuration. The originality of the approach proposed herein is to employ multiscale mechanical modeling approaches in order to understand the behavior of the AC implant in bone tissue and to determine the effect of the anisotropic biomechanical properties of bone tissue, which is a problem of clinical importance because bone properties depends on load transfer from the AC implant to peri-implant bone.

The choice of applying the loading conditions through the ancillary was made because of several reasons. First, it corresponds to a simple configuration compared to the complex interaction of the AC implant with the liner, which is out of scope of this study since we aim at studying the effect of bone properties on the mechanical behavior of the AC implant. Second, various loading scenarios may be applied to the ancillary during surgery when surgeons assess the AC implant stability manually. Third, we have already studied this configuration in a previous numerical study (in dynamic mode) and we eventually aim at assessing the loading distribution during impaction. The loading conditions were chosen in the range of loads used in experimental [2, 43, 44] and numerical studies [41, 42] and because it corresponds to typical stresses that can be applied *in vivo*. However, hip contact forces may sometimes be higher since they have been measured to be up to three times body weight under normal walking conditions [45]. Since all analyses are linear, the mechanical behavior of an AC implant subject to loading conditions with higher stresses can be derived from the results obtained herein using a simple linear extrapolation. Moreover, the mechanical

response of the system to a multiaxial loading can be obtained by a summation of the responses against three fundamental loading conditions presented in this paper.

The results shown in Fig. 3 indicate that the correlation coefficient of the linear regression analysis of the stiffness as a function of BV/TV is comprised between r^2=0.85 and 0.97, which indicates that BV/TV of the surrounding trabecular bone tissue may explain from 85% up to 97% of the AC implant stiffness, according to the loading condition considered. This correlation can be explained by the fact that the apparent Young's modulus *E* of trabecular bone is known to be highly correlated with BV/TV when measured according to the same direction of anisotropy, with determination coefficients typically around 0.85 [46]. However, the correlation between *E* and BV/TV is lower when all directions of testing are pooled (with a typical determination coefficient around 0.5 or lower [47, 48]) because of the influence of the anisotropic properties of trabecular bone tissue. In the present study, complex heterogeneous and multiaxial stress field is generated in bone tissue around the AC implant for each loading configuration described in subsection 2.3. Therefore, the overall stiffness of the bone-implant system is determined by a spatial averaging over the entire trabecular bone volume of the anisotropic local mechanical response of bone tissue. Such spatial averaging is realized over a multiaxial stress field, which explains the significant correlation with BV/TV since the effect of anisotropy has been integrated spatially. However, more samples are needed to compare the correlation coefficient obtained between the stiffness and BV/TV according to the loading conditions.

In order to understand the behavior of the AC implant rigidity, the relation between the maximum value of the von Mises stress obtained in the simulation domain and BV/TV was plotted in Fig. 4. The results are consistent with those obtained in Fig. 3 since the maximum von Mises stress is shown to increase when BVTV increases. However, the increase of the von Mises stresses as a function of BV/TV does not indicate an increase of fracture risk because bone strength is also known to increase with BVTV [49-51]. Moreover, the maximum of the Von Mises stresses (denoted $<\sigma_{Macro}>$ in what follows) indicated in Fig. 4 corresponds to macroscopic stresses, which can be related to the mean value of the microscopic (at the scale of the trabeculae) Von Mises stresses $<\sigma_{\mu}>$ through the simple following first order relationship:

$$<\sigma_{Macro}> = BV/TV * <\sigma_{\mu}>. \qquad (6)$$

The interest of determining $<\sigma_{\mu}>$ lies in the fact that $<\sigma_{\mu}>$ is an important determinant of possible microfractures at the scale of the trabeculae. Figure 10 shows the variation of $<\sigma_{\mu}>$ as a function of BV/TV for the four different loading conditions. The results show a significant decrease of the value of $<\sigma_{\mu}>$ as a function of BV/TV for the vertical and torsional loading configurations, which may indicate that bone

strength at the trabecular level might increase when BV/TV increases. However, such tendency was not found for the two horizontal loading configurations, which may be explained by the more complex and heterogeneous stress fields obtained in horizontal loading configurations. However, these results should be interpreted with caution due to the strong approximation employed in Eq. (6) and to the relatively low number of samples.

For all loading conditions and all samples, the maximum value of the von Mises stress field was always obtained on the bone-implant interface Γ_α^c, which emphasizes the critical importance of this interface for the implant outcome. Note that the fact that the maximum value of the von Mises stress is obtained at the bone-implant interface can also be seen in the results shown in Fig. 5. Figure 5 also shows that the stresses magnitude is the highest around the equatorial rim as well as in the polar area according to the loading scenario, which suggests important bone remodelling in these areas. More specifically, in the vertical loading configuration (Fig. 5a)), important levels of stresses were obtained around the rim periphery and around the cup dome. Figure 7a) shows that the compressive strains are mostly present around the cup dome, while Figs. 7b&d) indicate that shear strains (ε_{xz} and ε_{yz}) are dominant below the rim periphery. For the torsional loading condition (Fig. 5b)), important levels of stresses were obtained around the rim periphery. Figures 8b&d) show that the shear strains (ε_{xz} and ε_{yz}) are mostly present below the rim periphery. For the horizontal loading condition (along the *x*-axis) (Fig. 5c)), important levels of stresses were obtained around the rim periphery and around the cup dome. Figure 9 shows that the shear strains are significant below the rim periphery (ε_{xy}) and around the cup dome (ε_{xz}).

The stress field distributions shown in Fig. 5 and the strain field distributions shown in Figs. 7a) and 9b&d) are not axisymmetric compared to the *z*-axis, which is due to the anisotropic properties of trabecular bone. Similarly, the stress field distributions shown in Fig. 6 are not symmetric compared to the center of the image, which is also related to the anisotropy of trabecular bone.

The strain field distributions shown in Figs. 7b&d) are shown to be slightly different, although similar images are obtained when considering isotropic bone material properties (data not shown). Therefore, the difference in the two images shown in Figs. 7b&d) can also be explained by the bone anisotropy. The same explanation applies when comparing the images shown in Figs. 8b&d).

Another effect of bone anisotropy is shown in Figs. 7c), 8a&c) and 9c), where all corresponding strain field distributions are not equal to zero. We verified (data not shown), that for all the aforementioned

configurations, the corresponding strain fields are always equal to zero when considering isotropic bone properties. More quantitatively, in the case of vertical loading (Fig. 7), the magnitude of ε_{xz} is equal to around 3% (respectively 10%) of that of ε_{yz} (respectively ε_{xz}). In the case of torsional loading (Fig. 8), the magnitude of ε_{zz} is equal to around 10% of that of ε_{yz} and ε_{xz}. Eventually, in the case of horizontal loading (Fig. 9), the magnitude of ε_{xx} is equal to around 4% of that of ε_{xy} and ε_{xz}.

This study has several limitations. First, bovine bone samples were used, which have different biomechanical properties compared to human peri-implant bone. However, the range of BV/TV values is comprised in [0.11 , 0.44], which is similar to published values for human peri-implant bone [52] and thus bovine bone tissue was chosen to model human pelvis tissue. Moreover, a relatively low number of samples were considered, which is due to availability of the sample. However, the distribution of the BV/TV values cover a relatively wide range of variation.

Second, the procedure using the homogenization method employed in this study leads to uniform material properties around the implant, which constitutes a strong approximation since bone properties are likely to be heterogeneous around the implant. However, to the best of our knowledge, the heterogeneity of bone tissue around an AC implant has not been precisely quantified. Therefore, we chose to consider homogeneous bone properties and more work is needed to quantify bone heterogeneity and to investigate the effect of heterogeneous bone properties on the AC implant behavior. Moreover, we assumed that the main trabecular orientation is aligned with the z-axis, which corresponds to a simple approximation. More work would be required to determine the (possibly non homogeneous) orientation of the trabecular network around the AC implant, which is out of scope of the present study.

Third, the geometrical configuration is quite simple since cancellous and cortical bone geometry were chosen as hemispheric domains to model the hip configuration in a simple and reproducible manner. Different geometrical configurations have been used in the literature to model the AC implant biomechanical behavior. Some studies have considered bone as a 2D cylinder made of cancellous bone [20, 53], while others have integrated a cortical layer to represent the pelvic configuration [21, 54]. 3D finite element studies took into account the anatomy of the hip bone [16, 35, 55, 56]. We chose not to consider the anatomy of the acetabulum for the sake of simplicity and because the aim was to focus on the effect of trabecular bone properties in a standardized situation, which allows to simply investigate the effect of bone properties only on the AC implant mechanical behavior. Moreover, the ancillary was modeled by a 21 mm long bar in order to reduce the computation time and because it does not affect the results obtained in this study.

Fourth, the interface conditions between the implant and bone tissue were chosen as fully bonded over the entire bone-implant interface since the implant was considered as fully osseointegrated, similarly as what was done in [42]. However, interfacial parameters may affect the implant behavior [56] in particular

when considering stronger solicitations and/or healing interfaces, which is out of scope of the present study. Moreover, in clinical practice, polar gaps may occur [57] between the AC implant dome and the peri-implant bone and correspond to non-contact conditions in polar areas. Important polar gaps constitutes a critical clinical issue since osseointegration may not occur around this area [57]. Migration of the AC implant has even been observed for cases with polar gaps larger than 2 mm [58]. However, the influence of polar gap is out of scope of this study.

Fifth, we used an assumption of small displacements, which is justified by the relatively low amplitude of the strain field. As shown in Figs. 7 & 8, the magnitudes of the strain field obtained in the studied cases is always lower than 1.5 10-3, which justifies the assumption of small displacements. Using large displacement hypotheses and nonlinear analyses would be relevant to take into account sliding phenomena at the bone-implant interface, but it is out of scope of this paper and will be examined in future studies.

Sixth, in this paper, we focused mainly on the macroscopic behavior of the bone-implant system in relation with external forces. However, the results obtained at the macroscale can also be used using a downscaling analysis that allows to assess local behaviors of bone tissues at the microscale [32]. Such approach is useful to predict localized effects such as the stress concentration at trabeculae around the acetabular cup, and then to estimate the damage potential at the microscale. However, such analysis is out of scope of this study and further investigations need to be carried out in this direction in the future.

5. Conclusion

The present study investigates the influence the anisotropic properties of trabecular bone properties on the AC implant biomechanical behavior in a controlled configuration. It also shows that BV/TV is an important parameter determining the AC implant biomechanical behavior. The phenomena occurring around the equatorial rim and in the polar area are important for the AC implant mechanical behavior. The present approach may be used in the future to improve the design of the implant which should take into account the anisotropic biomechanical properties of the trabecular bone.

Appendix: Two-scale asymptotic homogenization method

The aim of this appendix is to describe the multiscale method employed to determine the effective anisotropic material properties of trabecular bone based on the 3D images of trabecular bone retrieved using the X-ray microcomputed tomography device (see subsection 2.1).

The method uses the principle of virtual work for the linear elastic problem described in Fig. 2, which can be written by:

$$\int_{\Omega_{ac}} C^{ac}_{ijkl} \frac{\partial u_i}{\partial x_j} \frac{\partial \overline{u}_k}{\partial x_l} d\Omega_{ac} + \int_{\Omega_c} C^{c}_{ijkl} \frac{\partial u_i}{\partial x_j} \frac{\partial \overline{u}_k}{\partial x_l} d\Omega_{c} + \int_{\Omega_t} C^{H}_{ijkl} \frac{\partial u_i}{\partial x_j} \frac{\partial \overline{u}_k}{\partial x_l} d\Omega_{t} = \int_{\Gamma^{\sigma}_{ac}} f_i \overline{u}_i d\Gamma^{ac}_{\sigma} \text{ , } \quad \text{(A.1)}$$

where u_i , $\overline{u}_k$ and f_i denotes the displacement, the virtual displacement and the traction, respectively. C^{H}_{ijkl} denotes the homogenized elastic tensor of trabecular bone, which is a symmetric forth order tensor representing the anisotropy. Note that the coordinates given in Fig. 2 are written by x_i in Eq. (A.1) to use the Einstein notations. The other notations follow the definition given in subsection 2.3.

The analysis of trabecular bone is carried out at the microscale based on μCT images. To do so, coordinates at the microscale defined by y_i are introduced. A scale ratio $\lambda = \frac{L}{l}$ is defined between macro- and microscales, where L and l are characteristic lengths associated respectively with macro- and microscales. The constitutive equation is defined at the microscale in the trabeculae by;

$$\sigma_{ij} = C^{c}_{ijkl} \varepsilon_{kl} \text{ , } \quad \text{(A.2)}$$

where σ_{ij} and ε_{kl} are the tensor components of microscopic stress and strain, respectively. The elastic tensor of bone tissue is given in Table 1. Therefore, the homogenized elastic tensor for the trabecular bone satisfies $\boldsymbol{C}^{H} = \left\langle \boldsymbol{C}^{bone} \right\rangle_t$ where $\langle \cdot \rangle_t$ indicates a volumetric average in the trabecular bone region influenced by its morphology. It can be calculated by:

$$C^{H}_{ijkl} = \frac{1}{|Y|} \int_Y \left(C^{c}_{ijkl} - C^{c}_{ijmn} \frac{\partial \chi^{kl}_m}{\partial y_n} \right) dY \text{ , } \quad \text{(A.3)}$$

where Y and $|Y|$ denote a representative volume element (RVE) of the microstructure in trabecular bone region and its volume, respectively. χ^{kl}_m is the characteristic displacement in the RVE, which forms the perturbed displacement due to microscopic heterogeneity and morphology. It is obtained by solving the following microscopic equations, which is associated with the self-equilibrium of the system:

$$\int_Y \left(C^{c}_{ijkl} - C^{c}_{ijmn} \frac{\partial \chi^{kl}_m}{\partial y_n} \right) \frac{\partial \overline{u}_i}{\partial y_j} dY = 0 \quad \text{(A.4)}$$

The above equations are derived by taking the limit of $\lambda \to 0$ for averaging, as described in more details in [29, 59].

This two-scale asymptotic homogenization theory has the advantage over micromechanics methods such as Mori-Tanaka scheme used in [39, 40] that arbitrary complex microarchitecture can be considered without any additional assumption. Moreover, such method is reliable has been validated experimentally by one of the authors by considering porous titanium [60], porous alumina [61], fiber reinforced plastics [62] and epoxy perforated plates [63]. The methods has also been validated experimentally in vertebral trabecular bone [64, 65]. Note that, in [65], stochastic analysis was performed, and the expected value of the stiffness coefficients coincides with the deterministic prediction used in this paper. However, one drawback of the asymptotic homogenization analysis is the computational cost when compared with the approaches based on micromechanics.

Acknowledgements

This work has been supported by French National Research Agency (ANR) through the PRTS program (project OsseoWave n°ANR-13-PRTS-0015-02).

The authors acknowledge the support of the Ecole Doctorale SIE of the UPE for the funding of AM in Keio University.

The authors acknowledge the help of Mr. Kyohei Hatano to run the computations.

This project has received funding from the European Research Council (ERC) under the European Union's Horizon 2020 research and innovation program (grant agreement No 682001, project ERC Consolidator Grant 2015 BoneImplant).

Bibliography

[1] A. Wengler, U. Nimptsch, and T. Mansky, "Hip and knee replacement in Germany and the USA: analysis of individual inpatient data from German and US hospitals for the years 2005 to 2011," *Dtsch Arztebl Int,* vol. 111, pp. 407-16, Jun 9 2014.

[2] J. T. Hsu, C. H. Chang, H. L. Huang, M. E. Zobitz, W. P. Chen, K. A. Lai*, et al.*, "The number of screws, bone quality, and friction coefficient affect acetabular cup stability," *Med Eng Phys,* vol. 29, pp. 1089-95, Dec 2007.

[3] K. A. Fehring, J. R. Owen, A. A. Kurdin, J. S. Wayne, and W. A. Jiranek, "Initial stability of press-fit acetabular components under rotational forces," *J Arthroplasty,* vol. 29, pp. 1038-42, May 2014.

[4] R. D. Bloebaum, N. L. Mihalopoulus, J. W. Jensen, and L. D. Dorr, "Postmortem analysis of bone growth into porous-coated acetabular components," *J Bone Joint Surg Am,* vol. 79, pp. 1013-22, Jul 1997.

[5] G. Haiat, H. L. Wang, and J. Brunski, "Effects of biomechanical properties of the bone-implant interface on dental implant stability: from in silico approaches to the patient's mouth," *Annu Rev Biomed Eng,* vol. 16, pp. 187-213, Jul 11 2014.

[6] L. A. Mueller, A. Kress, T. Nowak, D. Pfander, R. P. Pitto, R. Forst*, et al.*, "Periacetabular bone changes after uncemented total hip arthroplasty evaluated by quantitative computed tomography," *Acta Orthop,* vol. 77, pp. 380-5, Jun 2006.

[7] L. A. Mueller, R. Schmidt, C. Ehrmann, T. E. Nowak, A. Kress, R. Forst*, et al.*, "Modes of periacetabular load transfer to cortical and cancellous bone after cemented versus uncemented total hip arthroplasty: a prospective study using computed tomography-assisted osteodensitometry," *J Orthop Res,* vol. 27, pp. 176-82, Feb 2009.

[8] V. Mathieu, R. Vayron, G. Richard, G. Lambert, S. Naili, J. P. Meningaud*, et al.*, "Biomechanical determinants of the stability of dental implants: influence of the bone-implant interface properties," *J Biomech,* vol. 47, pp. 3-13, Jan 3 2014.

[9] K. Chiba, M. Ito, M. Osaki, M. Uetani, and H. Shindo, "In vivo structural analysis of subchondral trabecular bone in osteoarthritis of the hip using multi-detector row CT," *Osteoarthritis Cartilage,* vol. 19, pp. 180-5, Feb 2011.

[10] D. Ruffoni, A. J. Wirth, J. A. Steiner, I. H. Parkinson, R. Muller, and G. H. van Lenthe, "The different contributions of cortical and trabecular bone to implant anchorage in a human vertebra," *Bone,* vol. 50, pp. 733-8, Mar 2012.

[11] S. Matsunaga, Y. Shirakura, T. Ohashi, K. Nakahara, Y. Tamatsu, N. Takano*, et al.*, "Biomechanical role of peri-implant cancellous bone architecture," *Int J Prosthodont,* vol. 23, pp. 333-8, Jul-Aug 2010.

[12] T. Ohashi, S. Matsunaga, K. Nakahara, S. Abe, Y. Ide, Y. Tamatsu*, et al.*, "Biomechanical role of peri-implant trabecular structures during vertical loading," *Clin Oral Investig,* vol. 14, pp. 507-13, Oct 2010.

[13] S. E. Basler, J. Traxler, R. Muller, and G. H. van Lenthe, "Peri-implant bone microstructure determines dynamic implant cut-out," *Med Eng Phys,* vol. 35, pp. 1442-9, Oct 2013.

[14] W. Ma, X. Zhang, J. Wang, Q. Zhang, W. Chen, and Y. Zhang, "Optimized design for a novel acetabular component with three wings. A study of finite element analysis," *J Surg Res,* vol. 179, pp. 78-86, Jan 2013.

[15] A. T. Phillips, Pankaj, A. S. Usmani, and C. R. Howie, "The effect of acetabular cup size on the short-term stability of revision hip arthroplasty: a finite element investigation," *Proc Inst Mech Eng H,* vol. 218, pp. 239-49, 2004.

[16] D. Janssen, R. E. Zwartele, H. C. Doets, and N. Verdonschot, "Computational assessment of press-fit acetabular implant fixation: the effect of implant design, interference fit, bone quality, and frictional properties," *Proc Inst Mech Eng H,* vol. 224, pp. 67-75, 2010.

[17] P. Goebel, D. Kluess, J. Wieding, R. Souffrant, H. Heyer, M. Sander*, et al.*, "The influence of head diameter and wall thickness on deformations of metallic acetabular press-fit cups and UHMWPE liners: a finite element analysis," *J Orthop Sci,* vol. 18, pp. 264-70, Mar 2013.

[18] R. Ghosh, K. Mukherjee, and S. Gupta, "Bone remodelling around uncemented metallic and ceramic acetabular components," *Proc Inst Mech Eng H,* vol. 227, pp. 490-502, May 2013.

[19] S. D. Cook, K. A. Walsh, and R. J. Haddad, Jr., "Interface mechanics and bone growth into porous Co-Cr-Mo alloy implants," *Clin Orthop Relat Res,* pp. 271-80, Mar 1985.

[20] H. S. Hothi, J. J. Busfield, and J. C. Shelton, "Explicit finite element modelling of the impaction of metal press-fit acetabular components," *Proc Inst Mech Eng H,* vol. 225, pp. 303-14, Mar 2011.

[21] A. Yew, Z. M. Jin, A. Donn, M. M. Morlock, and G. Isaac, "Deformation of press-fitted metallic resurfacing cups. Part 2: Finite element simulation," *Proc Inst Mech Eng H,* vol. 220, pp. 311-9, Feb 2006.

[22] V. Mathieu, A. Michel, C. H. Flouzat Lachaniette, A. Poignard, P. Hernigou, J. Allain*, et al.*, "Variation of the impact duration during the in vitro insertion of acetabular cup implants," *Med Eng Phys,* vol. 35, pp. 1558-63, Jun 5 2013.

[23] A. Michel, R. Bosc, V. Mathieu, P. Hernigou, and G. Haiat, "Monitoring the press-fit insertion of an acetabular cup by impact measurements: influence of bone abrasion," *Proc Inst Mech Eng H,* vol. 228, pp. 1027-34, Oct 2014.

[24] A. Michel, R. Bosc, F. Sailhan, R. Vayron, and G. Haiat, "Ex vivo estimation of cementless acetabular cup stability using an impact hammer," *Med Eng Phys,* Dec 3 2015.

[25] A. Michel, R. Bosc, R. Vayron, and G. Haiat, "In vitro evaluation of the acetabular cup primary stability by impact analysis," *J Biomech Eng,* vol. 137, Mar 2015.

[26] S. Guipieri, Y. Nagatani, R. Bosc, V. H. Nguyen, C. Chappard, D. Geiger*, et al.*, "Ultrasound Speed of Sound Measurements in Trabecular Bone Using the Echographic Response of a Metallic Pin," *Ultrasound Med Biol,* vol. 41, pp. 2966-76, Nov 2015.

[27] S. J. Hollister and N. Kikuchi, "Homogenization theory and digital imaging: A basis for studying the mechanics and design principles of bone tissue," *Biotechnol Bioeng,* vol. 43, pp. 586-96, Mar 25 1994.

[28] J. M. Guedes and N. Kikuchi, "Preprocessing and postprocessing for materials based on the homogenization method with adaptive finite element method," *Comput Methods Appl Mech Eng,* vol. 83, pp. 143-198, 1990.

[29] J. L. Lions, *Some methods in the mathematical analysis of systems and their control*. New York 1981.

[30] R. Hart, "Bone modeling and remodeling: Theories and computation," in *Bone Mechanics Handbook*, S. C. Cowin, Ed., ed: CRC Press, 2001.

[31] T. C. T. Ting, *Anisotropic Elasticity. Theory and Applications.* : Oxford University Press, 1996.

[32] M. Tsukino, N. Takano, A. Michel, and G. Haïat, "Multiscale stress analysis of trabecular bone around acetabular cup implant by finite element mesh superposition method," *JSME MEL (Mechanical Engineering Letters),* vol. 1, pp. 15-00354, 2015.

[33] A. Michel, V. Nguyen, R. Bosc, R. Vayron, S. Naili, G. Haïat*, et al.*, "Finite element model of the impaction of a press-fitted acetabular cup," *Med Biol Eng Comput,* in press.

[34] Z. M. Lin, S. Meakins, M. M. Morlock, P. Parsons, C. Hardaker, M. Flett*, et al.*, "Deformation of press-fitted metallic resurfacing cups. Part 1: Experimental simulation," *Proc Inst Mech Eng H,* vol. 220, pp. 299-309, Feb 2006.

[35] R. Ghosh, S. Gupta, A. Dickinson, and M. Browne, "Experimental validation of finite element models of intact and implanted composite hemipelvises using digital image correlation," *J Biomech Eng,* vol. 134, p. 081003, Aug 2012.

[36] B. van Rietbergen, "Micro-FE analyses of bone: state of the art," *Adv Exp Med Biol,* vol. 496, pp. 21-30, 2001.

[37] V. Sansalone, S. Naili, V. Bousson, C. Bergot, F. Peyrin, J. Zarka*, et al.*, "Determination of the heterogeneous anisotropic elastic properties of human femoral bone: from nanoscopic to organ scale," *J Biomech,* vol. 43, pp. 1857-63, Jul 20 2010.

[38] V. Sansalone, V. Bousson, S. Naili, C. Bergot, F. Peyrin, J. D. Laredo*, et al.*, "Anatomical distribution of the degree of mineralization of bone tissue in human femoral neck: impact on biomechanical properties," *Bone,* vol. 50, pp. 876-84, Apr 2012.

[39] C. Hellmich, C. Kober, and B. Erdmann, "Micromechanics-based conversion of CT data into anisotropic elasticity tensors, applied to FE simulations of a mandible," *Ann Biomed Eng,* vol. 36, pp. 108-22, Jan 2008.

[40] Z. Yosibash, N. Trabelsi, and C. Hellmich, "Subject-Specific p-FE Analysis of the Proximal Femur Utilizing Micromechanics-Based Material Properties," *International Journal for Multiscale Computational Engineering,* vol. 6, pp. 483-498, 2008.

[41] I. R. Spears, M. Pfleiderer, E. Schneider, E. Hille, G. Bergmann, and M. M. Morlock, "Interfacial conditions between a press-fit acetabular cup and bone during daily activities: implications for achieving bone in-growth," *J Biomech,* vol. 33, pp. 1471-7, Nov 2000.

[42] C. Voigt, C. Klohn, R. Bader, G. von Salis-Soglio, and R. Scholz, "Finite element analysis of shear stresses at the implant-bone interface of an acetabular press-fit cup during impingement," *Biomed Tech (Berl),* vol. 52, pp. 208-15, Apr 2007.

[43] M. J. Curtis, R. H. Jinnah, V. D. Wilson, and D. S. Hungerford, "The initial stability of uncemented acetabular components," *Journal of Bone and Joint Surgery-British Volume,* vol. 74, pp. 372-376, May 1992.

[44] P. G. Perona, J. Lawrence, W. G. Paprosky, A. G. Patwardhan, and M. Sartori, "Acetabular micromotion as a measure of initial implant stability in primary hip arthroplasty. An in vitro comparison of different methods of initial acetabular component fixation," *J Arthroplasty,* vol. 7, pp. 537-47, Dec 1992.

[45] G. Bergmann, G. Deuretzbacher, M. Heller, F. Graichen, A. Rohlmann, J. Strauss*, et al.*, "Hip contact forces and gait patterns from routine activities," *J Biomech,* vol. 34, pp. 859-71, Jul 2001.

[46] G. Haiat, F. Padilla, M. Svrcekova, Y. Chevalier, D. Pahr, F. Peyrin*, et al.*, "Relationship between ultrasonic parameters and apparent trabecular bone elastic modulus: a numerical approach," *J Biomech,* vol. 42, pp. 2033-9, Sep 18 2009.

[47] P. Augat, T. Link, T. F. Lang, J. C. Lin, S. Majumdar, and H. K. Genant, "Anisotropy of the elastic modulus of trabecular bone specimens from different anatomical locations," *Med Eng Phys,* vol. 20, pp. 124-31, Mar 1998.

[48] J. P. van den Bergh, G. H. van Lenthe, A. R. Hermus, F. H. Corstens, A. G. Smals, and R. Huiskes, "Speed of sound reflects Young's modulus as assessed by microstructural finite element analysis," *Bone,* vol. 26, pp. 519-24, May 2000.

[49] R. W. Goulet, S. A. Goldstein, M. J. Ciarelli, J. L. Kuhn, M. B. Brown, and L. A. Feldkamp, "The relationship between the structural and orthogonal compressive properties of trabecular bone.," *J. Biomech.,* vol. 4, pp. 375-389, 1994.

[50] R. Hodsgkinson and J. D. Currey, "Seperate effects of osteoporosis and density on the strength and stiffness of human cancellous bone," *Clin. Biomech,* vol. 8, pp. 262-268, 1993.

[51] F. J. Hou, S. M. Lang, S. J. Hoshaw, D. A. Reimann, and D. P. Fyhrie, "Human vertebral body apparent and hard tissue stiffness.," *J. Biomech.,* vol. 31, pp. 1009-1015, 1998.

[52] D. R. Carter, R. Vasu, and W. H. Harris, "Periacetabular stress distributions after joint replacement with subchondral bone retention," *Acta Orthop Scand,* vol. 54, pp. 29-35, Feb 1983.

[53] C. Zietz, A. Fritsche, D. Kluess, W. Mittelmeier, and R. Bader, "Influence of acetabular cup design on the primary implant stability : an experimental and numerical analysis," *Orthopade,* vol. 38, pp. 1097-105, Nov 2009.

[54] I. R. Spears, M. M. Morlock, M. Pfleiderer, E. Schneider, and E. Hille, "The influence of friction and interference on the seating of a hemispherical press-fit cup: a finite element investigation," *J Biomech,* vol. 32, pp. 1183-9, Nov 1999.

[55] K. L. Ong, J. Lehman, W. I. Notz, T. J. Santner, and D. L. Bartel, "Acetabular cup geometry and bone-implant interference have more influence on initial periprosthetic joint space than joint loading and surgical cup insertion," *J Biomech Eng,* vol. 128, pp. 169-75, Apr 2006.

[56] I. R. Spears, M. Pfleiderer, E. Schneider, E. Hille, and M. M. Morlock, "The effect of interfacial parameters on cup-bone relative micromotions. A finite element investigation," *J Biomech,* vol. 34, pp. 113-20, Jan 2001.

[57] J. R. MacKenzie, J. J. Callaghan, D. R. Pedersen, and T. D. Brown, "Areas of contact and extent of gaps with implantation of oversized acetabular components in total hip arthroplasty," *Clin Orthop Relat Res,* pp. 127-36, Jan 1994.

[58] S. Nakasone, M. Takao, T. Nishii, T. Sakai, and N. Sugano, "Incidence and natural course of initial polar gaps in Birmingham Hip Resurfacing cups," *J Arthroplasty,* vol. 27, pp. 1676-82, Oct 2012.

[59] J. M. Guedes and N. Kikuchi, "Preprocessing and postprocessing for materials based on the homogenization method with adaptive finite element method," *Comput Methods Appl Mech Eng,* vol. 83, pp. 143-198, 1990.

[60] N. Takano, K. Fukasawa, and K. Nishiyabu, "Structural strength prediction for porous titanium based on micro-stress concentration by micro-CT image-based multiscale simulation," *Int J Mech Sci,* vol. 52, pp. 229-235, 2010.

[61] N. Takano, M. Zako, F. Kubo, and K. Kimura, "Microstructure-based stress analysis and evaluation for porous ceramics by homogenization method with digital image-based modeling," *Int J Solids Struct,* vol. 40, pp. 1225-1242, 2003.

[62] N. Takano, Y. Ohnishi, M. Zako, and K. Nishiyabu, "Microstructure-based deep-drawing simulation of knitted fabric reinforced thermoplastics by homogenization theory," *Int J Solids Struct,* vol. 38, pp. 6333-6356, 2001.

[63] T. Matsuda, T. Ito, S. Akimoto, H. Kobori, K. Goto, and N. Takano, "Macro/micro simultaneous validation for multiscale analysis of semi-periodically perforated plate using full-field strain measurement," *Int J Mech Sci,* vol. 110, pp. 34-40, 2016.

[64] Y. Yoshiwara, M. Clanche, K. S. Basaruddin, N. Takano, and T. Nakano, "Numerical study on the morphology and mechanical role of healthy and osteoporotic vertebral trabecular bone," *J Biomech Sci Eng,* vol. 6, pp. 270-285, 2011.

[65] K. S. Basaruddin, N. Takano, H. Akiyama, and T. Nakano, "Uncertainty modeling in the prediction of effective mechanical properties using stochastic homogenization method with application to porous trabecular bone," *54,* vol. Mat Trans, 2013.

[66] P. Henys, L. Capek, J. Fencl, and E. Prochazka, "Evaluation of acetabular cup initial fixation by using resonance frequency principle," *Proc Inst Mech Eng H,* vol. 229, pp. 3-8, Jan 2015.

Figure captions

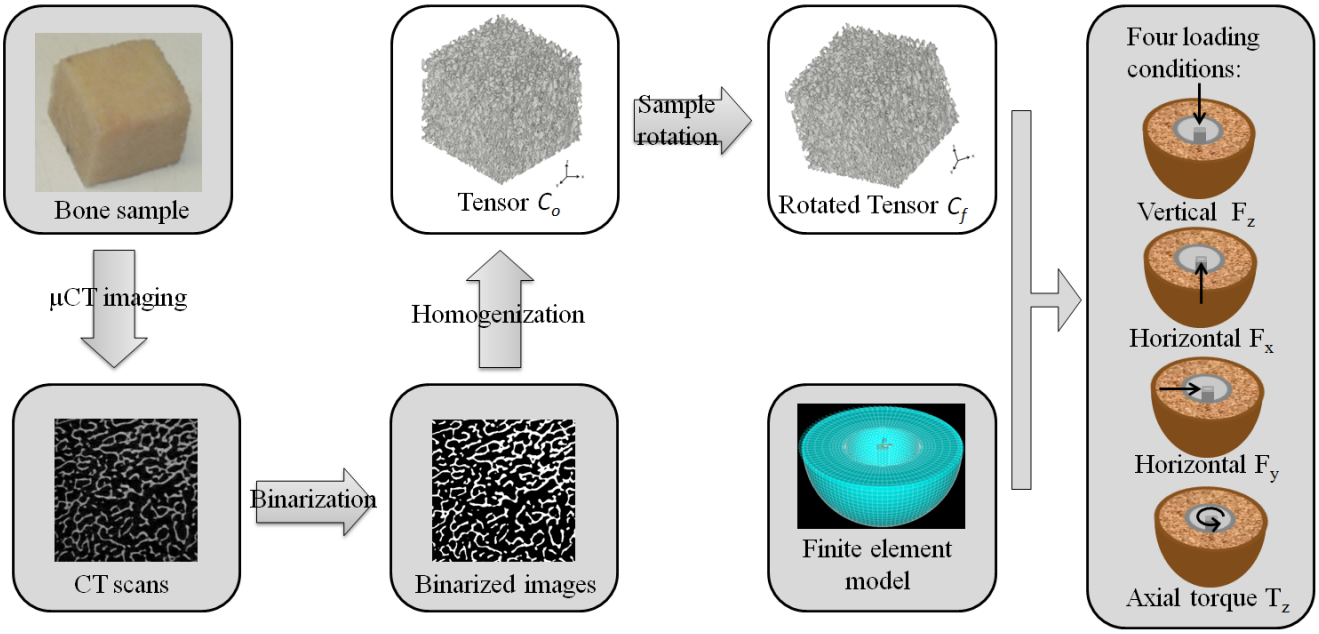

Figure 1 – Simulation procedure employed in the present study. Images obtained from microcomputed tomography scans were processed to determine the elasticity tensor of the trabecular bone sample. This elasticity tensor was then rotated and used in the finite element model. Four loading conditions were studied.

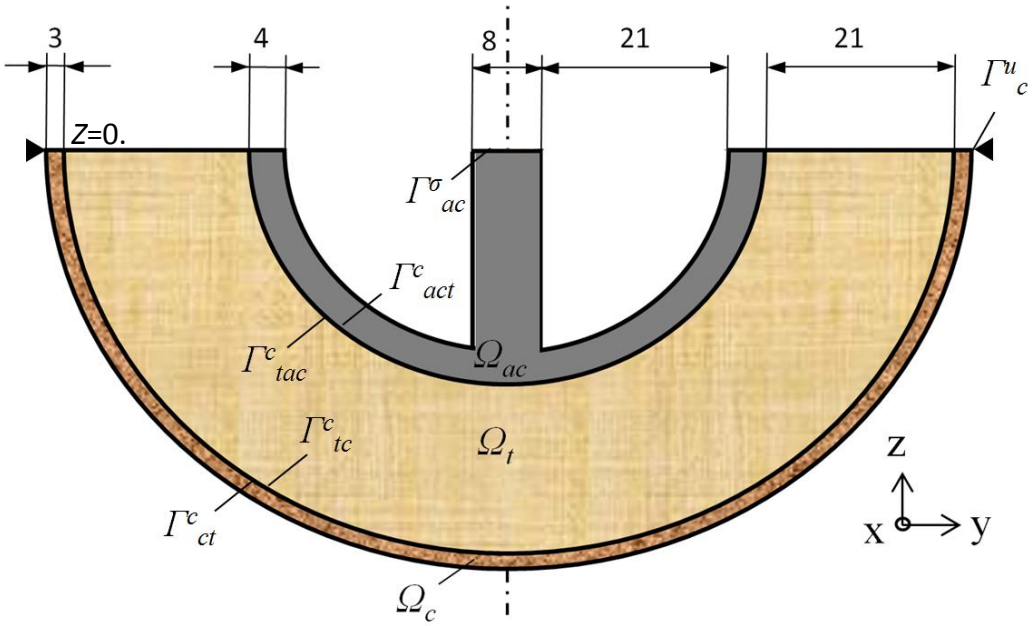

Figure 2 - Cross-section of the geometrical configuration (lengths are expressed in mm) considered in the 3D finite element model. The black triangles represent the fixation of the outer circle of cortical bone denoted by Γ^u_c

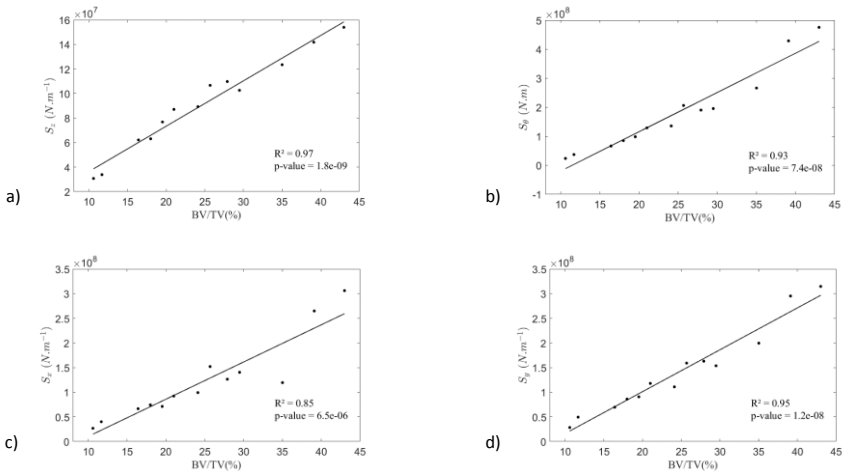

Figure 3 - Macroscopic stiffness values as a function of BV/TV for all data pooled for: a) the vertical loading (S_z), b) the torsional loading (S_θ), the horizontal loading along the x-axis (S_x) and d) the horizontal loading along the y-axis (S_y).

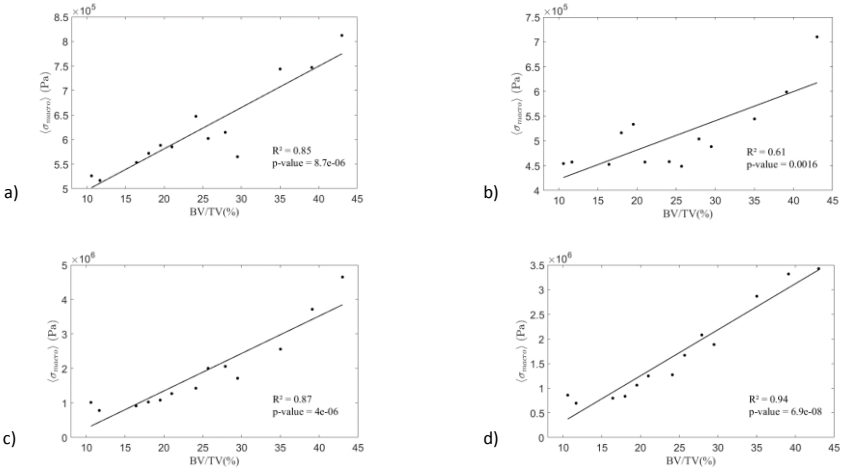

Figure 4 – Variation of the maximum of the von Mises stress $<\sigma_{Macro}>$ obtained in the entire trabecular region (Ω_t) and BV/TV in the case of a) vertical loading, b) torsional loading, c) horizontal loading along the *x*-axis and d) horizontal loading along the *y*-axis. The maximum value of the von Mises stress was obtained on the bone-implant interface for all samples and all loading configurations.

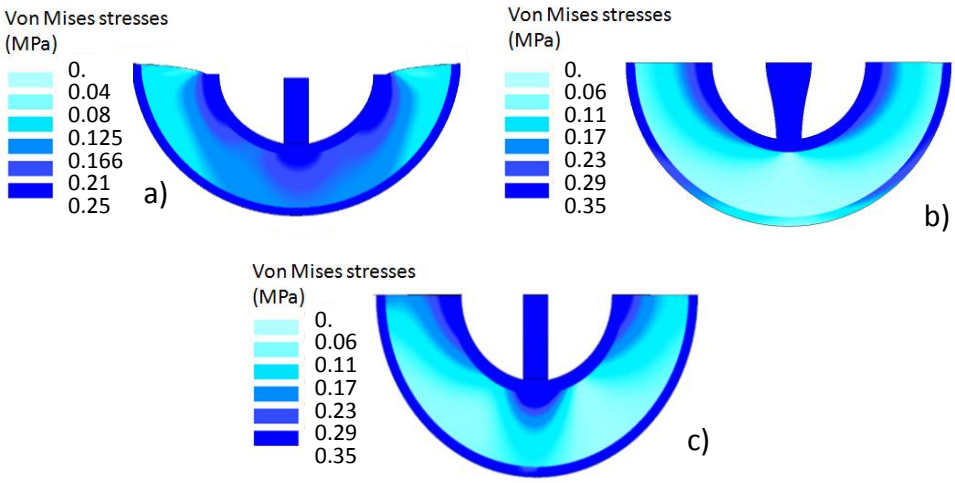

Figure 5 - Cross-sectional view in the plane Π_{yz} of the strain field in the implant and in the peri-implant bone for a bone sample (BV/TV=18.0%) under a) vertical loading F_z, b) torsional loading T_z and c) horizontal loading F_x.

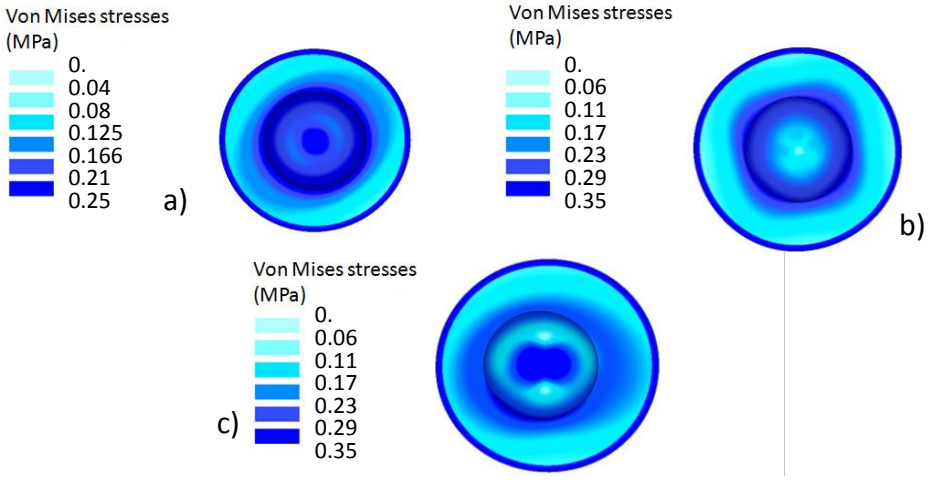

Figure 6 - Cross-sectional of the Von-Mises stresses (MPa) in the plane Π_{xy} corresponding z= -26.5 mm for a given sample (BV/TV = 18.0%) under a) vertical loading F_z, b) axial torque T_z and c) horizontal loading in the x-axis. In the outer ring, the field of the von Mises stresses in bone tissue is shown. In the inner region, the color codes the projection of the

von Mises stresses obtained at the bone-implant interface located under Π_{xy} (i.e. for z<-26.5 mm) on Π_{xy}.

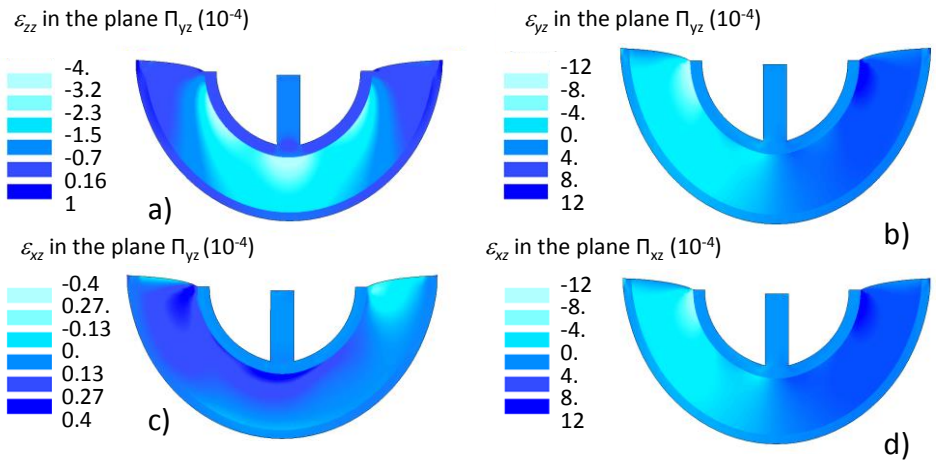

Figure 7 - Cross-sectional view of the strain field in the implant and in the peri-implant bone for a bone sample (BV/TV=18.0%) under vertical loading for a) ε_{zz} in the plane Π_{yz}, b) ε_{xz} in the plane Π_{yz}, c) ε_{yz} in the plane Π_{yz} and d) ε_{xz} in the plane Π_{xz}.

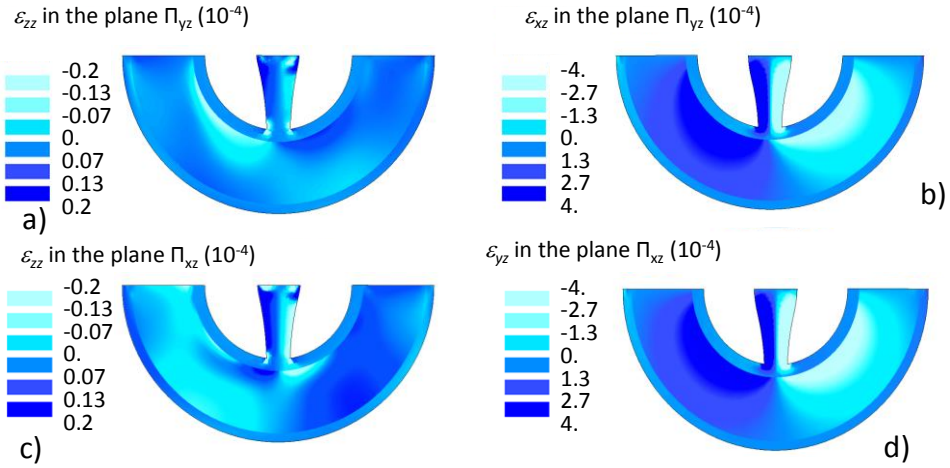

Figure 8 - Cross-sectional view of the strain field in the implant and in the peri-implant bone for a bone sample (BV/TV=18.0%) under torsional loading for a) ε_{zz} in the plane Π_{yz}, b) ε_{xz} in the plane Π_{yz}, c) ε_{zz} in the plane Π_{xz} and d) ε_{yz} in the plane Π_{xz}.

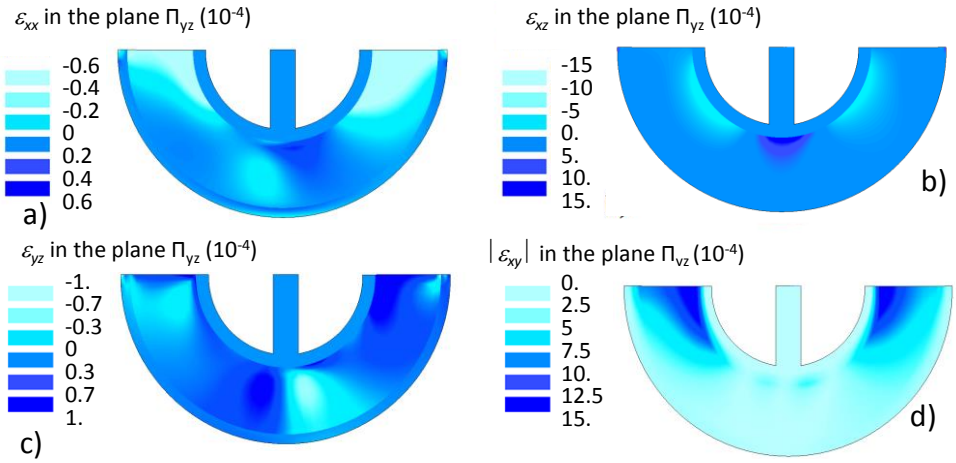

Figure 9 - Cross-sectional view in the plane Π_{yz} of the strain field in the implant and in the peri-implant bone for a bone sample (BV/TV=18.0%) under horizontal loading along the *x*-axis for a) ε_{xx}, b) ε_{xz}, c) ε_{yz} and d) ε_{xy}.

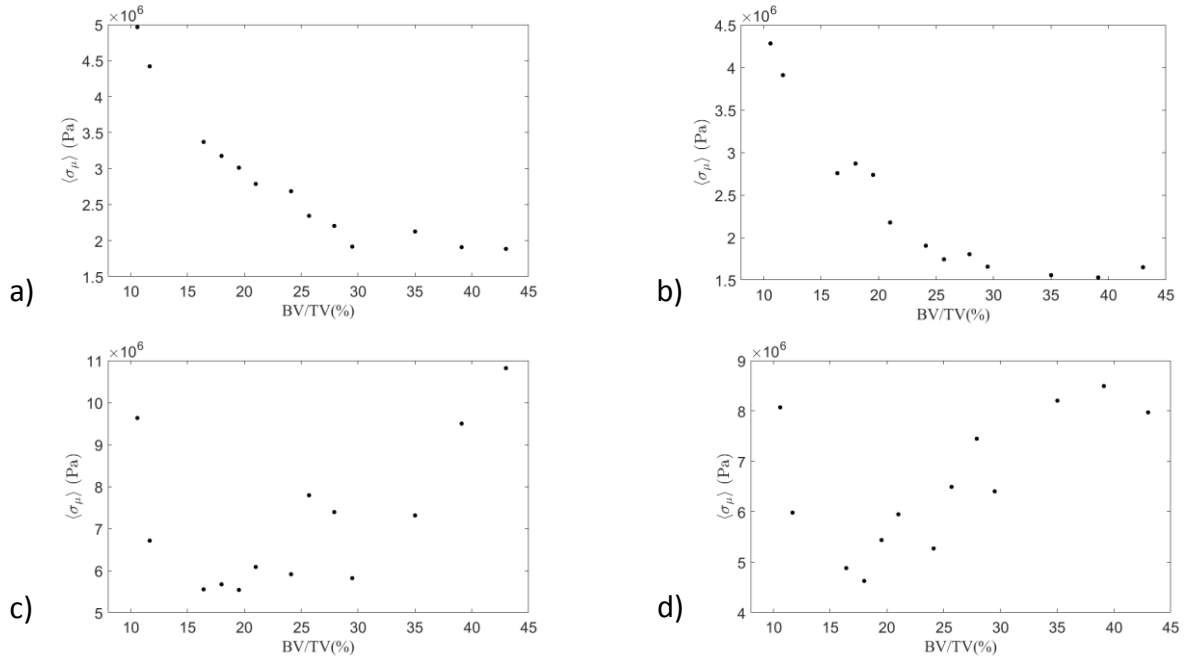

Figure 10 - Variation of the maximum of the von Mises stress divided by BV/TV $<\sigma_\mu>$, (which corresponds to an approximation of the Von Mises stress at the scale of the trabeculae) as a function of BV/TV in the case of a) vertical loading, b) torsional loading, c) horizontal loading along the *x*-axis and d) horizontal loading along the *y*-axis.

Table 1. Mechanical properties of materials.

Material	Young's modulus (MPa)	Poisson's ratio	References
Cortical bone	15000	0.3	[34, 35, 56, 66]
Co-Cr	210000	0.3	[21]